RSC Advances

ROYAL SOCIETY OF CHEMISTRY

PAPER

View Article Online
View Journal | View Issue

Check for updates

Cite this: *RSC Adv.*, 2026, **16**, 22514

New hybrid compound $(C_6H_{10}N_2)(H_2PO_4)_2$: insights into its structural, optical, and electrical behavior for electronic applications

Arafet Ghoudi,[a] Najoua Weslati,[a] Nourah A. Alsobai,[b] Noweir Ahmad Alghamdi,[c] Walid Rekik[d] and Abderrazek Oueslati*[a]

Received 13th November 2025
Accepted 7th April 2026

DOI: 10.1039/d5ra08777e

rsc.li/rsc-advances

This study reports the synthesis, structural analysis, and optical and electrical characterization of a novel organic–inorganic hybrid compound: *o*-phenylenediammonium bis(dihydrogenophosphate) $(C_6H_{10}N_2)(H_2PO_4)_2$. Single-crystal X-ray diffraction analysis reveals that the compound crystallizes in the triclinic system within the centrosymmetric space group $P\bar{1}$. Its crystal structure is stabilized by a three-dimensional hydrogen-bonding network involving both N–H⋯O and O–H⋯O interactions, which significantly enhance the material's structural cohesion and interionic connectivity. Optical characterization *via* UV–Visible spectroscopy demonstrates strong light absorption and reveals a direct optical band gap of 2.13 eV, suggesting promising potential for optoelectronic applications. In parallel, complex impedance spectroscopy highlights favorable electrical and dielectric behavior over various frequencies and temperatures. The AC conductivity of the polycrystalline sample was found to follow Jonscher's universal power law. Moreover, the asymmetrical shape of the imaginary part of the electric modulus, analyzed using the Kohlrausch–Williams–Watts (KWW) model, confirms the presence of non-Debye relaxation dynamics. The material exhibits a remarkably high dielectric permittivity ($\varepsilon' \approx 8 \times 10^4$), underscoring its strong potential for energy storage applications. These results underline the strong interplay between the compound's electrical and optical properties, positioning it as a promising multifunctional material for future electronic, photonic, and energy-related applications.

1 Introduction

The study of charged species, particularly cations and anions, has emerged as a significant area of interest in both organic chemistry and biological sciences.[1] These ionic entities play essential structural roles in mediating molecular associations and stabilizing the tertiary conformations of biomolecules such as proteins and nucleic acids.[2] Among the various families of compounds, those involving monophosphate anions paired with highly polarizable organic cations have received considerable attention.[2–5] One of the most distinctive characteristics of these materials is the dense hydrogen-bonding network formed around the monophosphate units, which are often surrounded by numerous hydrogen-bond donors.[6] Hydrogen bonding has been widely recognized as a key factor influencing not only crystal packing and stability[7] but also the emergence of nonlinear optical properties in phosphate-based materials.[8,9] In recent years, organic–inorganic monophosphate salts have been extensively investigated due to their potential in various functional applications. In these systems, phosphoric anions are typically interconnected through strong hydrogen bonds, forming infinite anionic frameworks with diverse structural topologies. A notable example is the compound $(C_{12}H_{19}N_2)H_2PO_4\cdot H_2O$,[10] which crystallizes in the monoclinic space group $P2_1/c$ ($Z = 4$) with lattice parameters $a = 15.226(2)$ Å, $b = 6.984(3)$ Å, $c = 15.359(5)$ Å, and $\beta = 95.44(2)°$. Its crystal structure features $(H_4P_2O_8)^{2-}$ dimers that associate with water molecules through hydrogen bonding to form layered inorganic networks. These layers are interleaved with $(C_{12}H_{19}N_2)^+$ cations, which participate in both van der Waals interactions and strong hydrogen bonds with the oxygen atoms of the anionic layers. Another example is *meta*-carboxyphenylammonium phosphite (*m*-CPAMP), $(C_7H_8NO_2)H_2PO_3$, whose structure has been investigated across a temperature range of 100–345 K.[2] A first-order phase transition was identified at 246 K by Bendeif *et al.*,[11] attributed to structural changes in the molecular configuration. In yet another case, the cyanostar–phosphate complex[12] displays a stack of four cyanostar macrocycles threaded by three hydrogen phosphate anions, forming

---

[a] Laboratory for Spectroscopic Characterization and Optics of Materials, Faculty of Sciences, University of Sfax, B. P. 1171, 3000 Sfax, Tunisia. E-mail: arafetghoudi199@gmail.com

[b] Department of Physics, College of Science, Taif University, P.O. Box 11099, Taif, 21944, Saudi Arabia

[c] Department of Physics, Faculty of Science, Al-Baha University, Alaqiq, 65779, Saudi Arabia

[d] Laboratory Physical-Chemistry of Solid State, Chemistry Department, Faculty of Sciences of Sfax, University of Sfax, BP 1171, 3000, Sfax, Tunisia

a trianionic trimer assembly $[H_2PO_4\cdots H_2PO_4\cdots H_2PO_4]^{3-}$ stabilized by hydrogen bonding. The average O⋯O separation of 2.57 Å between phosphate units indicates the presence of strong, directional hydrogen bonds. Considering the pivotal role of hydrogen bonding in shaping the chemical and structural properties of such systems, the present work is dedicated to the synthesis and characterization of a new hybrid material based on *o*-phenylenediammonium and phosphoric acid. We report the synthesis, crystal structure, and investigation of the optical and electrical properties of the novel compound *o*-phenylenediammonium bis(dihydrogenophosphate).

2 Experimental section

2.1. Synthesis and crystal growth

Single crystals of the hybrid compound $(C_6H_{10}N_2)(H_2PO_4)_2$ were obtained by slow evaporation of an aqueous solution. In a typical synthesis, *o*-phenylenediamine (1 mmol, 0.108 g) was dissolved in 20 mL of demineralized water under continuous stirring at room temperature. Subsequently, phosphoric acid (2 mmol, 0.196 g of H_3PO_4 solution) was added dropwise to the solution. The resulting mixture was stirred for approximately 30 min until a clear homogeneous solution was obtained.

The solution was then filtered and left to evaporate slowly at ambient temperature (∼298 K) under undisturbed conditions. After about 5–7 days, colorless transparent crystals suitable for single-crystal X-ray diffraction were formed. The crystals were collected by filtration and dried at room temperature. The reaction yield was approximately 78%. The obtained crystals were visually free of impurities and exhibited good morphological quality.

This synthesis approach follows a procedure similar to those reported for related hybrid dihydrogen phosphate materials,[13,14] with slight modifications in reagent proportions and crystallization conditions.

2.2. Single-crystal diffraction data collection and structure determination

Single-crystal diffraction data for $(C_6H_{10}N_2)(H_2PO_4)_2$ were collected for a high-quality single-crystal with a four-circle BRUKER APEX II area-detector diffractometer ($\lambda = 0.71073$ Å). Intensity data were collected at 296(2) K through the APEX 2 program.[15] An Empirical absorption correction of multi-scan type was performed with the SADABS program.[16] The title compound adopts triclinic symmetry and crystallizes in the centrosymmetric space group $P\bar{1}$, according to the ShelxT-2018 program[17] integrated into the WINGX interface.[18] The structure solution was developed by successive difference Fourier syntheses and refined by full-matrix least-squares on all $|F|^2$ data using the ShelxL-2014 program.[19] Hydrogen atoms linked to oxygen atoms were located in the difference Fourier map, and their positions and isotropic displacement parameters were refined. In contrast, the hydrogen atoms of the organic moiety were placed geometrically and allowed to ride on their parent atoms with N–H = 0.89 Å and C–H = 0.93 Å, using the HFIX instruction available in the ShelxL-2014 program.[19] All drawings of the crystal structure were made using the Diamond3.2 program.[20] The crystallographic data and the experimental details of the structure determination and final refinements are summarized in Table 1. The fractional atomic coordinates and

Table 1 Crystal data and structure refinement parameters for $(C_6H_{10}N_2)(H_2PO_4)_2$

Formula	$(C_6H_{10}N_2)(H_2PO_4)_2$
Color/shape	Colorless/prism
Formula weight (g mol^{-1})	304.13
Crystal system	Triclinic
Space group	$P\bar{1}$
Density	1.756
Crystal size (mm)	0.23 × 0.19 × 0.14
Temperature (K)	296(2)
Diffractometer	Bruker APEXII CCD
a (Å)	6.7147(3)
b (Å)	9.8221(5)
c (Å)	10.1044(6)
α	66.861(3)
β (°)	73.272(2)
γ	73.338(3)
V (Å^3)	575.35(5)
Z	2
Radiation type	Mo $K\alpha$ (0.71073 Å)
Absorption correction	Multi-scan
θ range for data collection (°)	$2.237 \leq \theta \leq 28.526$
Measured reflections	21 646
Independent reflections	2914
Observed data [$I > 2\sigma(I)$]	2475
Index ranges	$h = -8 \rightarrow 9$
	$k = -13 \rightarrow 13$
	$l = -13 \rightarrow 13$
F (000)	316
Number of parameters	181
R_1	0.0355
wR_2	0.0938
Goof	1.038

Table 2 Fractional atomic coordinates and equivalent isotropic temperature factors (Å^2)

	x	Y	z	U_{eq}
C1	0.7554(3)	0.5347(3)	−0.0742(2)	0.0375(5)
C2	0.8213(3)	0.3870(3)	−0.0710(2)	0.0391(5)
C3	0.8395(3)	0.2705(2)	0.0607(2)	0.0315(4)
C4	0.7915(3)	0.3030(2)	0.18869(19)	0.0211(3)
N1	0.81436(2)	0.17963(17)	0.32795(18)	0.0267(3)
N2	0.6627(2)	0.48501(17)	0.32221(17)	0.0246(3)
C7	0.7214(3)	0.45104(19)	0.18620(19)	0.0202(3)
C8	0.7041(3)	0.5676(2)	0.0539(2)	0.0288(4)
P1	0.22099(7)	0.24993(5)	0.49933(5)	0.01938(12)
O1	0.1894(2)	0.13008(17)	0.65826(15)	0.0335(3)
O2	0.0049(2)	0.30143(15)	0.45955(14)	0.0269(3)
O3	0.3287(2)	0.36658(15)	0.49198(15)	0.0297(3)
O4	0.3778(2)	0.16280(17)	0.39643(17)	0.0310(3)
P2	0.66398(7)	0.09056(5)	0.77567(5)	0.02296(13)
O5	0.7763(2)	0.0295(2)	0.90893(18)	0.0440(4)
O6	0.4286(2)	0.09685(19)	0.83070(14)	0.0367(4)
O7	0.6935(2)	0.25839(15)	0.69674(16)	0.0314(3)
O8	0.7741(2)	0.00427(18)	0.67265(18)	0.0417(4)

Table 3 Selected bond distances (Å) and angles (°)

Distances (Å)		Angles (°)	
C1–C2	1.381(3)	C2–C1–C8	120.46(19)
C1–C8	1.381(3)	C1–C2–C3	120.16(19)
C2–C3	1.383(3)	C4–C3–C2	119.54(19)
C3–C4	1.380(3)	C3–C4–C7	120.44(17)
C4–C7	1.386(2)	C3–C4–N1	119.50(17)
C4–N1	1.465(2)	C7–C4–N1	120.06(16)
N2–C7	1.459(2)	C8–C7–C4	119.85(17)
C7–C8	1.386(2)	C8–C7–N2	119.68(16)
P1–O3	1.4898(13)	C4–C7–N2	120.46(15)
P1–O2	1.5093(13)	C1–C8–C7	119.52(19)
P1–O1	1.5719(14)	O3–P1–O2	118.15(8)
P1–O4	1.5730(15)	O3–P1–O1	110.99(8)
P2–O8	1.4966(15)	O2–P1–O1	105.03(8)
P2–O6	1.5087(14)	O3–P1–O4	106.24(8)
P2–O5	1.5596(16)	O2–P1–O4	109.51(8)
P2–O7	1.5671(15)	O1–P1–O4	106.39(9)
		O8–P2–O7	116.89(9)
		O8–P2–O5	109.75(10)
		O6–P2–O5	109.51(8)
		O8–P2–O7	108.82(9)
		O6–P2–O7	106.28(9)
		O5–P2–O7	104.86(9)

Table 4 Hydrogen bonding geometry (Å, °)[a]

D—H···A	D—H	H···A	D···A	D—H···A
N1–H1A···O4	0.89	2.01	2.845(2)	155.4
N1–H1B···O2^{ii}	0.89	1.95	2.822(2)	165.3
N1–H1C···O1^{iii}	0.89	2.41	2.996(2)	123.9
N1–H1C···O8^{i}	0.89	2.12	2.839(2)	137.1
N2–H2A···O7^{iv}	0.89	2.23	2.922(2)	134.8
N2–H2B···O2^{ii}	0.89	1.98	2.819(2)	155.9
N2–H2C···O3	0.89	1.77	2.653(2)	173.1
O1–H41B···O6	0.90(3)	1.67(3)	2.5661(19)	176(3)
O4–H31···O8^{iii}	0.81(3)	1.74(3)	2.547(2)	171(3)
O7–H6···O2^{ii}	0.81(3)	1.86(3)	2.669(2)	172(3)
O5–H5···O6^{V}	0.78(3)	1.81(3)	2.585(2)	173(3)

[a] Symmetry codes: ^{i} $-x+2, -y, -z+1$; ^{ii} $x+1, y, z$; ^{iii} $-x+1, -y, -z+1$; ^{iv} $-x+1, -y+1, -z+1$; ^{v} $-x+1, -y, -z+2$.

equivalent isotropic temperature factors are presented in Table 2. Selected bond distances and angles and hydrogen bonds are shown in Tables 3 and 4, respectively.

2.3. Instrumentation and methodologies for morphological, UV-visible, and complex impedance analyses

The elemental composition and chemical nature of the synthesized compound were thoroughly investigated using energy-dispersive X-ray spectroscopy (EDX), performed with a Bruker Quantax 100 Easy EDX detector.

The optical properties of the compound were investigated using a Shimadzu UV-3101PC UV-Vis-NIR spectrophotometer. The measurements were carried out in both absorbance and diffuse reflectance modes using a LISR-3100 integrating sphere attachment. A $BaSO_4$ standard was employed as the reference material for reflectance measurements. The spectra were recorded with a slit width of 20 nm over the selected wavelength range under ambient laboratory conditions. The sample was finely ground before analysis to ensure uniform optical response and reliable spectral acquisition.

The electrical properties of the compound were investigated using complex impedance spectroscopy. The measurements were performed using a precision Solartron 1260 frequency response analyzer over a frequency range from 10^2 to 10^6 Hz. The sample was prepared in pellet form (8 mm in diameter and 1.1 mm thick) by pressing the powdered material into a circular disk under uniaxial pressure. Both surfaces of the pellet were coated with a thin layer of silver paste to ensure good electrical contact and to form blocking electrodes.

The impedance measurements were carried out in the temperature range of 358–398 K using a temperature-controlled chamber with an accuracy of ±1 K. The temperature was stabilized for approximately 10 min at each measurement point before recording the impedance spectra to ensure thermal equilibrium.

3 Results and discussion

3.1. Structure description

The hybrid compound investigated in this work has the chemical formula $(C_6H_{10}N_2)(H_2PO_4)_2$, consisting of a doubly protonated *o*-phenylenediammonium cation $(C_6H_{10}N_2)^{2+}$ associated with two dihydrogen phosphate anions $(H_2PO_4)^-$. The asymmetric unit, shown in Fig. 1, contains one doubly protonated *o*-phenylenediammonium cation and two dihydrogen phosphate anions. All atoms of the asymmetric unit occupy general positions in the crystal lattice (Wyckoff site: 2i).

The *o*-phenylenediammonium bis(dihydrogenophosphate) $(C_6H_{10}N_2)(H_2PO_4)_2$, adopts the triclinic symmetry and crystallizes at 296(2) K in the centrosymmetric $P\bar{1}$ space group with the following unit cell parameters: $a = 6.7147(3)$ Å; $b = 9.8221(5)$ Å;

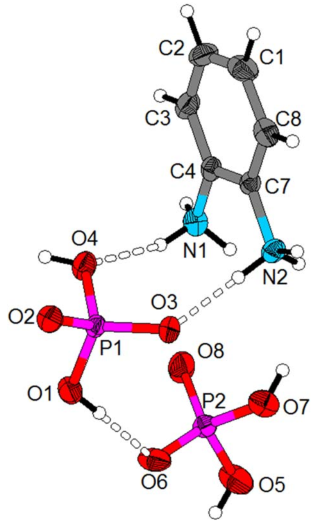

Fig. 1 Asymmetric unit of $(C_6H_{10}N_2)(H_2PO_4)_2$. Displacement ellipsoids are drawn at the 50% probability level. Hydrogen bonds are represented as dashed lines.

$c = 10.1044(6)$ Å; $\alpha = 66.861(3)°$; $\beta = 73.272(2)°$; $\gamma = 73.338(3)°$; $V = 575.35(5)$ Å^3 and $Z = 2$. Its 0D structure is built of isolated dihydrogenophosphate anions and protonated diamine $(C_6H_{10}N_2)^{2+}$. The structure cohesion is established by N–H⋯O and O–H⋯O hydrogen bonds (Fig. 2).

The asymmetric unit contains two crystallographically independent phosphorus atoms, each of which is surrounded by two terminal oxygen atoms and two hydroxyl groups to form the dihydrogenphosphate anion $(H_2PO_4)^-$. The main bond lengths P–O and angles O–P–O in these inorganic anions are given in Table 3. It should be noted that the short distances (1.4898(13) Å and 1.5093(13) Å for H_2P1O_4 and 1.4966(15) Å and 1.5087(14) Å for H_2P2O_4) are attributed to the terminal P–O bonds, whereas the longer distances (1.5719(14) Å and 1.5730(15) Å for H_2P1O_4 and 1.5596(16) Å and 1.5671(15) Å for H_2P2O_4) correspond to P–OH bonds of the hydroxyl groups.[21] Within these inorganic anions, the O–P–O angles vary between 105.03(8) and 118.15(8)° for H_2P1O_4 and between 104.86(9) and 116.89(9)° for H_2P2O_4 (Table 3). These geometrical characteristics of $(H_2PO_4)^-$ anions are in good agreement with those observed in other compounds containing the dihydrogenophosphate groups,[22–24] confirming that the phosphate tetrahedra maintain the typical distortion commonly encountered in hydrogen-bonded phosphate frameworks.

To better position the present material within the family of organic–inorganic dihydrogenophosphate hybrids, a comparison with structurally related compounds is useful. In several previously reported organic monophosphates, $(H_2PO_4)^-$ anions associate through hydrogen bonds to form extended inorganic networks.[10,13,14,25,26] For example, in $(C_{12}H_{19}N_2)H_2PO_4 \cdot H_2O$, the $(H_2PO_4)^-$ anions aggregate in pairs to form $[(H_4P_2O_8)^{2-}]$ units, which, together with water molecules, generate inorganic layers parallel to the plane $x = 1/2$.[10] The organic cations, derived from piperazine in this case, are inserted between these layers and establish additional N–H⋯O hydrogen bonds with the phosphate groups. Similarly, in $(FC_6H_4CH_2NH_3)H_2PO_4$ (4-fluorobenzylammonium dihydrogen phosphate), the PO_4 tetrahedra are linked *via* O–H⋯O hydrogen bonds, forming corrugated layers parallel to the ab plane,[27] while aromatic cations occupy the regions between inorganic layers. Another example is the salt 2-aminobenzamide · H_2PO_4, where $(H_2PO_4)^-$ anions form $[(H_4P_2O_8)^{2-}]$ dimers separated by organic ion dimers connected through multiple hydrogen bonds.[28] These examples illustrate the structural richness of dihydrogenophosphate-based materials, where chains, layers, or cage-like architectures may arise depending on the arrangement of the O–H⋯O hydrogen bonds, highlighting the versatility of phosphate units in determining crystal network dimensionality.[10,28]

As seen in Fig. 2 and 3, the dihydrogenophosphate anions are stacked so that they form anionic layers parallel to the *ac*-plane at $y = 0$ and $y = 1$. Within the inorganic layers, the dihydrogenophosphate anions are linked together through strong O–H⋯O hydrogen bonds. Indeed, within these intermolecular bonds, the O⋯O distances are between 2.547(2) and 2.669(2) Å and the O–H⋯O angles range from 171(3) to 176(3)° (Table 4).

The negative charges of the dihydrogenophosphate anions $(H_2PO_4)^-$ are compensated by the doubly protonated diamine cations $(C_6H_{10}N_2)^{2+}$. As shown in Fig. 2, these protonated diamines are arranged in such a way that they form an organic cationic layer parallel to the *ac*-plane at $y = 1/2$. Consequently, the crystal structure of $(C_6H_{10}N_2)(H_2PO_4)_2$ can be described as an alternation along the crystallographic *b*-axis of organic cationic layers, built from protonated diamines $(C_6H_{10}N_2)^{2+}$,

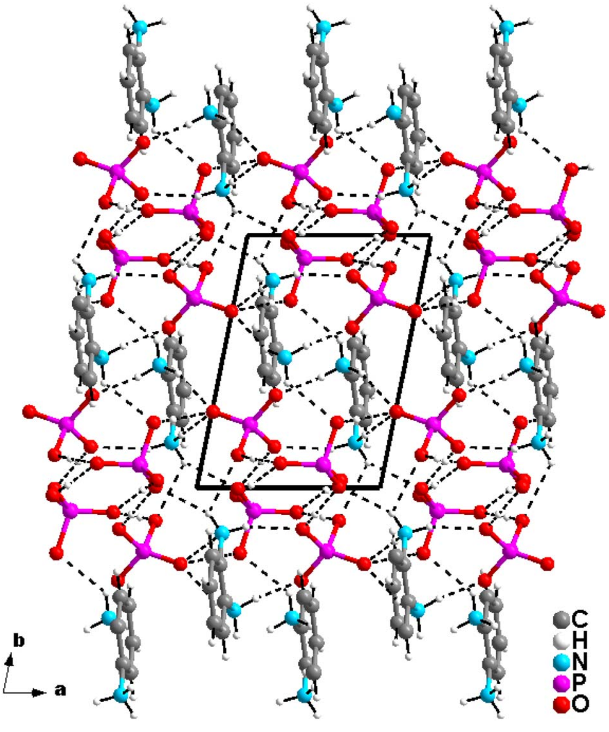

Fig. 2 Projection of the structure of $(C_6H_{10}N_2)(H_2PO_4)_2$ along the crystallographic *c*-axis.

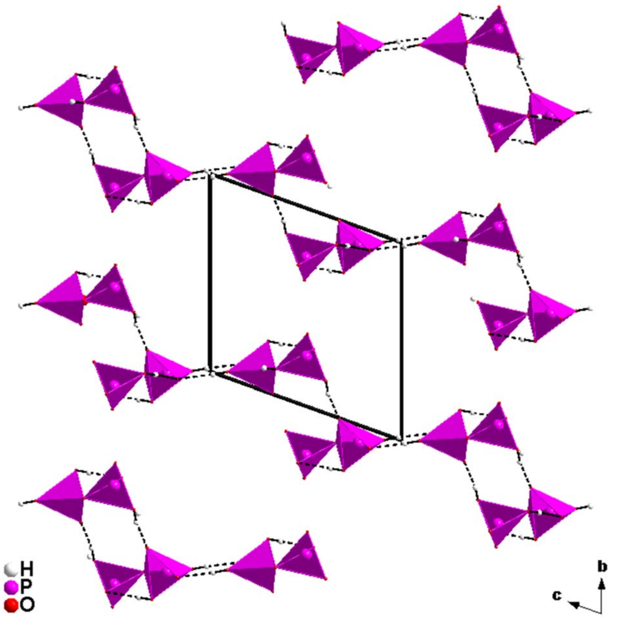

Fig. 3 Projection of the inorganic group structure along the crystallographic *a*-axis.

and inorganic anionic layers parallel to the (0 1 0) plane composed of dihydrogenophosphate anions $(H_2PO_4)^-$. The main bond distances and angles of the organic cations are summarized in Table 3.

The protonated diamine cations $(C_6H_{10}N_2)^{2+}$ are further stabilized by π–π interactions involving a parallel-displaced configuration arrangement of adjacent aromatic rings.[29,30] The shortest centroid–centroid distance between two parallel aromatic rings is 3.5407(2) Å (Fig. 4), confirming the presence of significant aromatic stacking interactions.

The aromatic *o*-phenylenediammonium cation, therefore, provides additional stabilization through π–π interactions, complementing the N–H⋯O hydrogen bonds established with the phosphate framework. A similar situation has been reported in the 2,4,6-trimethylpyridinium dihydrogen phosphate salt, where pyridinium cations align *via* π–π stacking interactions (centroid–centroid distance = 3.46 Å), forming parallel chains within the structure.[31] Such π–π interactions between aromatic rings are well known to enhance structural cohesion and increase the rigidity of crystal packings by reinforcing the organic–inorganic network.[31] In the present compound, the combined effect of N–H⋯O hydrogen bonds and π–π stacking interactions acts cooperatively to strengthen the overall crystal structure, a feature that is less common in phosphate hybrids containing non-aromatic cations.

On the other hand, the protonated diamine cations are linked to the dihydrogenophosphate anions through an extensive N–H⋯O hydrogen bonding network. Indeed, each protonated diamine uses its nitrogen-bound hydrogen atoms to establish N–H⋯O hydrogen bonds with five neighboring $(H_2PO_4)^-$ anions (Fig. 5). Within these intermolecular interactions, the N⋯O distances range from 2.653(2) to 2.996(2) Å, while the N–H⋯O angles vary between 123.9° and 173.1° (Table 4), indicating hydrogen bonds of variable strength that contribute significantly to the stabilization of the three-dimensional supramolecular framework. The cooperative effect between O–H⋯O bonds linking phosphate units and N–H⋯O interactions connecting organic and inorganic components generates a highly interconnected structure, ensuring strong coupling between the two sublattices.

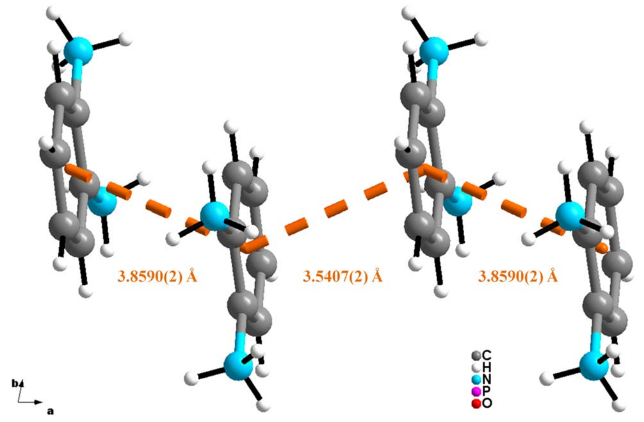

Fig. 4 π–π interactions in the structure of $(C_6H_{10}N_2)(H_2PO_4)_2$.

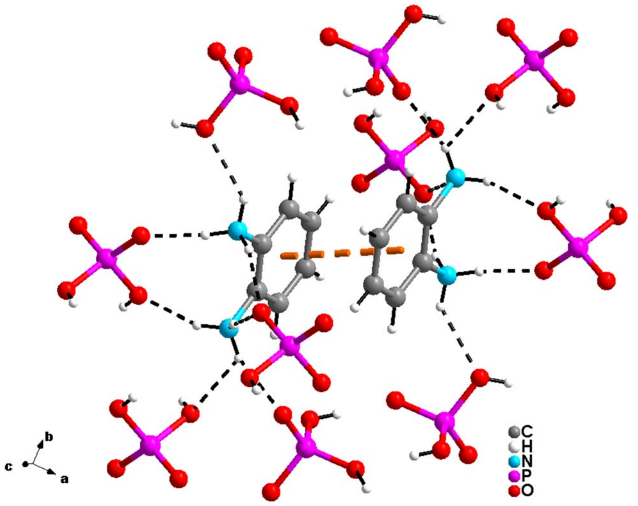

Fig. 5 Hydrogen bonds established by the protonated diamine in $(C_6H_{10}N_2)(H_2PO_4)_2$.

From a structure–property perspective, comparison with analogous phosphate-based hybrids highlights the key role of crystal organization in governing functional behavior. While several organic dihydrogenophosphate materials exhibit conventional dielectric responses and moderate electrical conductivity,[23] the present compound displays pronounced non-Debye relaxation behavior together with relatively high conductivity and high dielectric permittivity. This difference can be rationalized by the structural arrangement: the dense hydrogen-bonded network of $(H_2PO_4)^-$ units interconnected through O–H⋯O interactions, combined with the compact stacking of aromatic cations, favors localized charge hopping and interfacial polarization effects. In other words, the observed electrical properties arise directly from the crystal architecture, namely, the extended hydrogen-bond network and the cooperative influence of aromatic interactions, rather than from chemical composition alone. This contrast highlights the importance of considering phosphate network topology when interpreting and predicting the functional properties of hybrid phosphate systems.

3.2. EDX results

The EDX spectrum, presented in Fig. 6, clearly displays distinct and well-defined peaks corresponding to carbon (C), phosphate (P), nitrogen (N), and oxygen (O). Each of these peaks represents the specific energy levels associated with the respective elements, confirming their presence in the synthesized compound. The quantitative analysis yields: C (35.46 wt%, 43.14 at%), N (16.02 wt%, 16.71 at%), O (39.08 wt%, 35.69 at%), and P (9.44 wt%, 4.45 at%). These values are consistent with the expected stoichiometric ratios within the semi-quantitative accuracy of EDX measurements. The lower atomic percentage of phosphorus reflects its proportion in the total number of atoms in the molecular formula and does not indicate compositional deficiency.

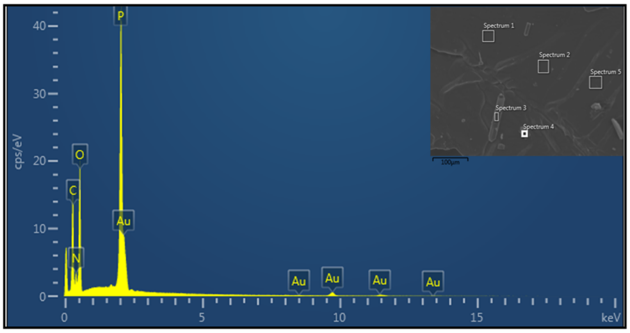

Fig. 6 EDX analysis of $(C_6H_{10}N_2)(H_2PO_4)_2$.

Moreover, minor peaks of gold (Au) were also detected in the spectrum. These do not correspond to the compound's intrinsic composition but are instead attributed to the thin gold coating applied to the sample surface before EDX analysis.[32] This coating process is a standard preparation step aimed at enhancing surface conductivity and preventing charging effects under the electron beam, thus ensuring improved spectral quality and signal accuracy.

Overall, the EDX results confirm the expected elemental composition of the material, further supporting the successful formation of the desired hybrid compound.

3.3. Optical properties

The optical response of hybrid organic–inorganic materials is strongly influenced by their crystal architecture, intermolecular interactions, and electronic coupling between organic and inorganic building units.[33] In this study, the optical investigation of $(C_6H_{10}N_2)(H_2PO_4)_2$ was carried out not only to determine its band-gap energy but also to establish a correlation between its structural organization and the electronic transitions governing its optical behavior.

Fig. 7 presents the UV-Vis-NIR absorption spectrum of $(C_6H_{10}N_2)(H_2PO_4)_2$. The spectrum shows a distinct absorption region in the 700–1000 nm wavelength range, followed by a nearly constant low-absorption region, which is characteristic of semiconducting hybrid systems in which the optical response arises from both the inorganic phosphate framework and the organic aromatic cations.[33,34] The shoulder features observed near the absorption edge should be considered intrinsic to the material rather than measurement artefacts. In hybrid molecular systems, the coexistence of aromatic units, phosphate groups, and extended hydrogen-bonding networks may generate localized electronic states and band-tail absorption, which commonly appear as shoulder features in UV-Vis spectra.

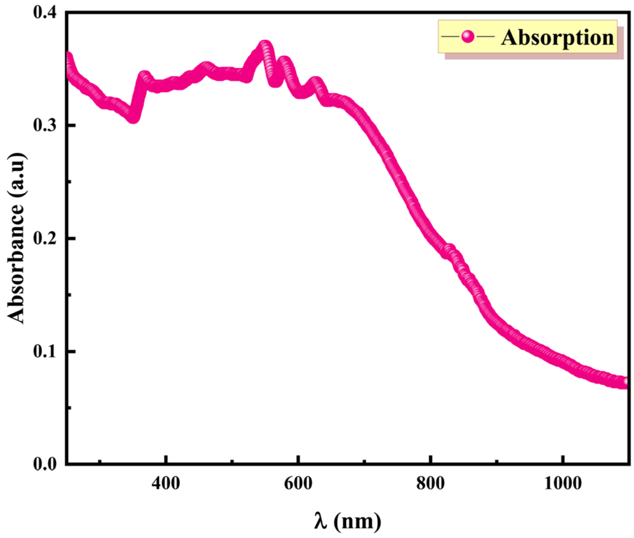

Fig. 7 UV-Vis spectra of $(C_6H_{10}N_2)(H_2PO_4)_2$.

From an orbital perspective, the optical absorption of the studied compound can be mainly attributed to transitions involving the electronic states of the aromatic *o*-phenylenediammonium cations and their interaction with the surrounding phosphate environment. The aromatic rings provide delocalized π orbitals, while non-bonding lone-pair electrons located on nitrogen and oxygen atoms introduce *n* states. Therefore, the absorption edge can be associated with a combination of π–π^* transitions within the aromatic system and n–π^* transitions involving lone-pair orbitals coupled to antibonding π^* states. Similar orbital contributions have been reported in aromatic-phosphate hybrid materials, where the optical response is dominated by transitions originating from aromatic molecular orbitals influenced by hydrogen bonding and inorganic surroundings.[35] These interactions can slightly perturb the frontier orbitals and contribute to the observed shoulder features.

The optical band gap is commonly extracted using the Tauc method, based on the following relationship:[36]

$$F(R) = \frac{(1-R)^2}{2R} \tag{1}$$

$$[F(R)h\nu]^{1/n} = A(h\nu - E_g) \tag{2}$$

where R denotes the reflectance percentage, $h\nu$ represents the photon energy, and E_g corresponds to the optical band gap energy. The terms A and n are constants, where n takes the value of 1/2 for direct transitions and 2 for indirect ones. In semiconductors with a direct band gap ($n = 1/2$), photon absorption and emission occur through allowed transitions without the need for momentum change. Conversely, in indirect band-gap materials, the processes of absorption and recombination involve both photons and phonons to conserve momentum, as illustrated in Fig. 8.

The band gap of $(C_6H_{10}N_2)(H_2PO_4)_2$ can be determined using eqn (2). As depicted in the inset of Fig. 9, the Tauc plot derived from the absorption spectrum of $(C_6H_{10}N_2)(H_2PO_4)_2$ allows the estimation of E_g values. Through linear extrapolation, the band gap is found to be approximately 2.13 eV for a direct transition ($n = 1/2$) and 1.84 eV for an indirect transition ($n = 2$).

To accurately determine the band gap, it is essential first to identify the nature of the transition. According to the findings of Marotti, Henrique, and their collaborators,[37,38] E_g can be estimated from the reflectance spectrum, $R(\lambda)$, particularly by

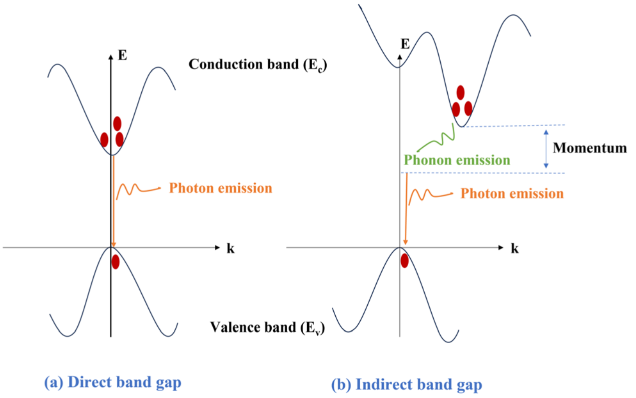

Fig. 8 : Direct and indirect band gaps.

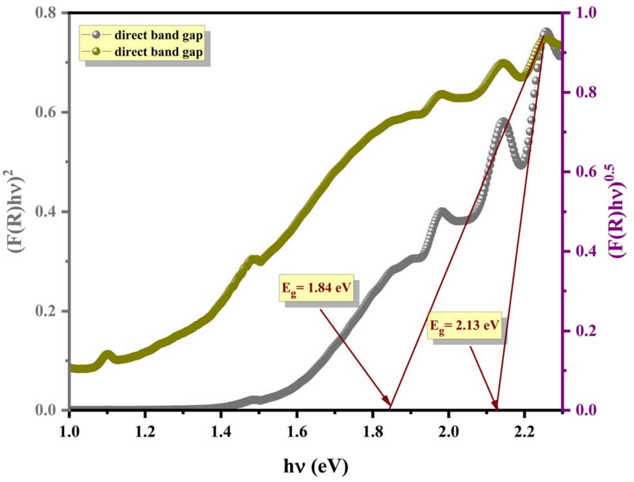

Fig. 9 Tauc plots for $(C_6H_{10}N_2)(H_2PO_4)_2$.

locating the maximum of the function $(1/R(\lambda)) \times (dR(\lambda)/d\lambda)$. As illustrated in Fig. 10, the compound $(C_6H_{10}N_2)(H_2PO_4)_2$ exhibits a significant peak around 559 nm. Applying the standard relation between photon energy and wavelength, $E(\text{eV}) = \dfrac{1240}{\lambda(\text{nm})}$, the band gap is estimated to be approximately 2.21 eV. This value closely matches that obtained for $n = 1/2$, confirming that the compound exhibits a direct-type band gap. Such a band gap is consistent with those found in typical semiconducting materials, particularly those with relatively narrow band gaps. Interestingly, this E_g is larger than that reported for $C_{11}H_{17}N_4 \cdot H_2PO_4$ (1.33 eV),[39] but smaller than that of $(C_6H_{10}N_2)_2MnCl_6 \cdot 2H_2O$ (2.71 eV).[40]

The differences in band-gap values among these compounds can be attributed to variations in the crystal structure, intermolecular interactions, and the electronic coupling between the organic cations and the inorganic framework, which influence the frontier molecular orbitals involved in the optical transitions.

From a physical perspective, assigning a direct allowed transition is reasonable for this molecular crystal. The structure consists of alternating inorganic dihydrogenophosphate layers and protonated aromatic diammonium cations interconnected through an extended hydrogen-bonding network.[7–9] Such an arrangement promotes electronic coupling between neighboring structural units and reduces momentum constraints during optical excitation. In addition, π–π stacking interactions between aromatic rings[29,30] enhance orbital overlap and facilitate charge delocalization within the organic layers. In molecular crystals, where electronic bands are generally weakly dispersed, optical transitions commonly occur between localized frontier orbitals (HOMO–LUMO type),[39] making direct transitions more probable than indirect ones. Therefore, the structural characteristics of the compound provide a physically consistent explanation for the observed direct allowed transition.

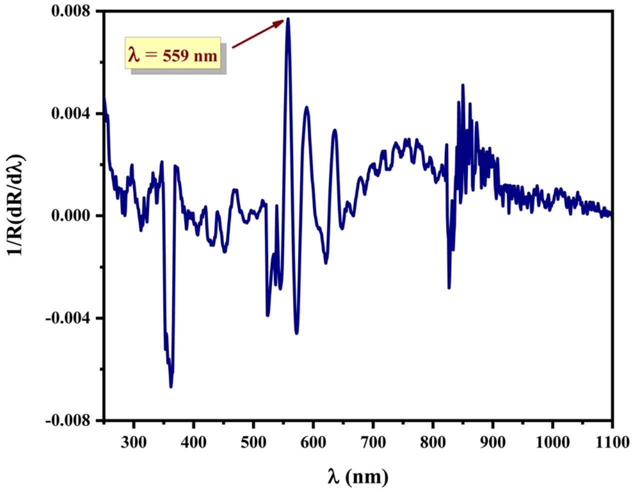

Fig. 10 Variation of $(1/R(\lambda))(dR(\lambda)/d\lambda)$ as a function of wavelength for the hybrid compound $(C_6H_{10}N_2)(H_2PO_4)_2$.

The measured band gap is thus not merely an isolated optical parameter but reflects the cooperative effect of hydrogen bonding, organic–inorganic layering, and aromatic interactions within the crystal lattice. This demonstrates that the optical properties of $(C_6H_{10}N_2)(H_2PO_4)_2$ arise from its specific supramolecular organization, highlighting a clear structure–property correlation. Such understanding is important for the rational design of hybrid phosphate materials, where optical absorption and electronic behavior can be tuned through structural engineering.

Overall, the combination of a direct band gap and strong structural cohesion indicates that this hybrid compound is a promising candidate for optoelectronic applications, where controlled intermolecular interactions play a key role in optimizing optical performance.

3.4. Electrical properties

The electrical behavior of hybrid organic–inorganic materials is strongly governed by their structural organization, particularly hydrogen-bond networks, interfacial heterogeneity, and molecular packing effects, which collectively influence charge transport and dielectric polarization mechanisms.[41,42]

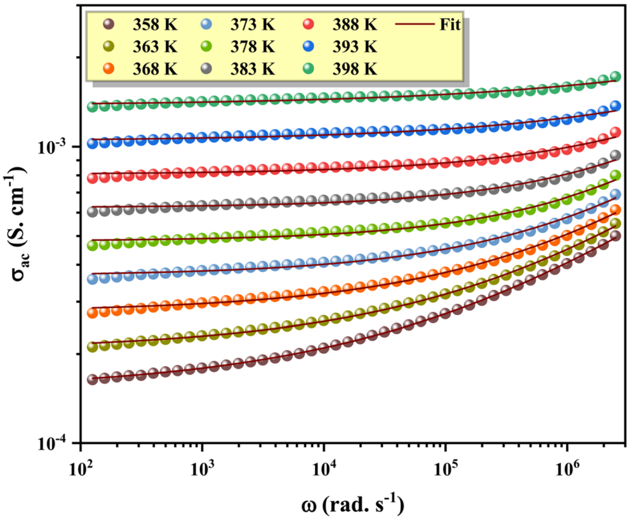

Fig. 11 Frequency dependence of the ac conductivity σ_{ac} at various temperatures for the $(C_6H_{10}N_2)(H_2PO_4)_2$ compound.

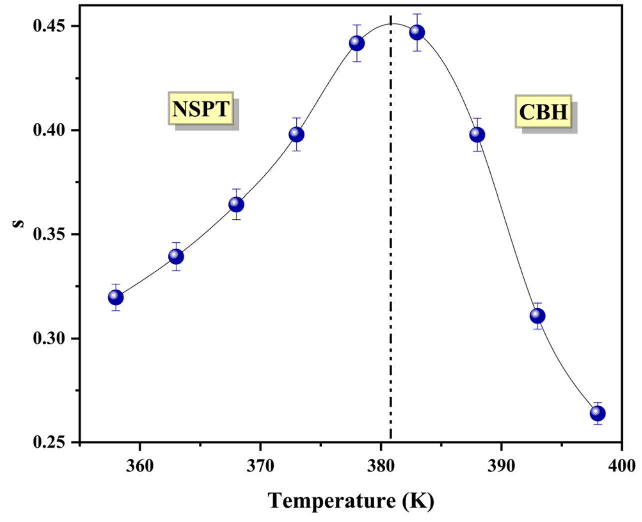

Fig. 12 Temperature evolution of the s parameter.

3.4.1. AC electrical conductivity and conduction mechanism analysis. The analysis of AC conductivity was carried out to better understand how the material's electrical properties respond to changes in frequency. The relationship between AC conductivity and frequency serves as a valuable tool for identifying the nature of the charge carriers.[43] Fig. 11 displays the variation of σ_{ac} with frequency at different temperatures. The studied hybrid compound demonstrates conductivity values ranging from 10^{-4} to 10^{-3} S cm^{-1}, supporting its classification as a semiconductor. As shown in Fig. 10, the conductivity spectra reveal two characteristic regions. In the low-frequency domain (100–10^4 rad s^{-1}), σ_{ac} appears nearly constant, indicating frequency independence and suggesting a thermally activated process that intensifies as temperature rises, likely due to the DC component.[44–46] At higher frequencies, the σ_{ac} curve reveals a dispersion region. These are attributed to charge carriers within the grains gaining sufficient energy to surmount potential barriers across short distances. Under these conditions, the behavior of the compound conforms to Jonscher's universal power law:[42]

$$\sigma_{ac} = \sigma_{dc} + A\omega^{s} \tag{3}$$

where, σ_{dc} represents the direct current conductivity observed at low frequencies, while A is a parameter influenced by temperature. The exponent s, which lies between 0 and 1, characterizes the extent of interaction between charge carriers and their surrounding environment.

From the fitting of the experimental AC conductivity data using Jonscher's power law, important information can be extracted from the temperature dependence of the frequency exponent s, as illustrated in Fig. 12. The exponent s is a key parameter in AC conductivity analysis because it provides insight into the dominant charge-transport mechanism in the material.[41,47] In particular, its value and temperature evolution allow the identification of the conduction model governing the electrical response, such as correlated barrier hopping (CBH) mechanism (s decreases with temperature), quantum mechanical tunneling (QMT) (s stays close to 0.8 and/or increases slightly with temperature), non-overlapping small polaron tunneling (NSPT) (s increases with temperature), and overlapping large polaron tunneling (OLPT) (s decreases until a minimum value and then increases upon temperature increase).[48–51]

As shown in Fig. 12, the variation of s reveals two distinct thermal regions, indicating a change in the dominant conduction mechanism.

- In the range 358 $K \leq T \leq$ 383 K, the value of s increases with temperature. This behavior aligns with the non-overlapping small polaron tunneling (NSPT) model. If we denote τ_0 as the characteristic relaxation time and W_H as the polaron hopping energy, then s is given by the following relation:[52]

$$s(T) = 1 + \frac{4}{\frac{W_H}{k_B T} - \ln(\omega\tau_0)} \tag{4}$$

when W_H/k_BT becomes significantly large, this expression for s can be simplified.

$$s(T) = 1 + \frac{4k_BT}{W_H} \tag{5}$$

- For temperatures in the interval 383 K $\leq T \leq$ 398 K, s decreases as temperature rises, which is indicative of the correlated barrier hopping (CBH) mechanism governing the conductivity in this range. In this regime, the expression for s is provided by ref. 53,

$$s(T) = 1 - \frac{6k_BT}{W_M + k_BT\,\ln(\omega\tau_0)} \tag{6}$$

and under the condition $W_M >> k_BT\ln(\omega\tau_0)$, the relation simplifies accordingly.

$$s(T) = 1 - \frac{6k_BT}{W_M} \tag{7}$$

The crossover temperature (383 K) was identified from the maximum of the $s(T)$ curve, where the temperature dependence of the frequency exponent changes from increasing to decreasing. This turning point indicates a transition from NSPT behavior at lower temperatures to a CBH mechanism at higher temperatures, reflecting a change in the dominant charge-transport regime. Physically, this transition arises from the increase in thermal energy, which progressively reduces carrier localization and facilitates hopping over potential barriers.

The linear dependence of the parameter (1 s) on temperature was used to estimate the activation energies associated with the conduction process. The extracted values of W_M and W_H are 0.04 eV and 0.06 eV, respectively. These relatively low activation energies indicate that the electrical conduction is dominated by localized short-range hopping rather than long-range band transport. This behavior is consistent with the crystal structure of the compound, in which the extended O–H⋯O hydrogen-bonded phosphate network forms continuous pathways that facilitate charge transfer between closely spaced localized states. As a result, charge carriers require only small energy barriers to move within the hydrogen-bonded framework.

Moreover, the coexistence of hydrogen-bonded inorganic units and organic cations creates a heterogeneous energy landscape that supports both tunneling and barrier-hopping processes, thereby explaining the transition between NSPT and CBH mechanisms. The fact that s remains below unity throughout the studied temperature range further supports a hopping-dominated conduction mechanism,[54,55] consistent with Funke's jump-relaxation model.[56]

3.4.2. DC conductivity study.

Fig. 13 illustrates an affine plot of $\ln(\sigma_{dc})$ *versus* $1000/T$, which follows the Arrhenius equation.

$$\sigma_{dc} = \sigma_0 \exp\left(-\frac{E_a}{k_B T}\right) \tag{8}$$

where σ_0 is the pre-exponential factor, k_B is the Boltzmann constant, and E_a is the activation energy.

By applying this linear model, the activation energy (E_a) was estimated to be 0.67 (±0.03) eV within the temperature range of 358 to 398 K. This result highlights that the charge transport is driven by a thermally activated hopping mechanism. The electrical conductivity of the studied compound, ranging from 10^{-4} to 10^{-3} S cm^{-1} is notably higher than that of the hybrid compound $[C_{12}H_{13}N_2O]H_2PO_4$, whose conductivity lies between 10^{-8} and 10^{-4} S cm^{-1} (for $T = 291$–393 K).[3] This difference can be attributed to structural variations between the two materials, particularly their organic components. In $[C_{12}H_{13}N_2O]H_2PO_4$, the hydrogen-bonding network is arranged differently compared to our compound. Likely, hydrogen atoms are more easily delocalized in the current material, thereby enhancing charge mobility and contributing to higher conductivity. This inference is further supported by the lower activation energy found in our compound compared to that of $[C_{12}H_{13}N_2O]H_2PO_4$, which has $E_a > 1$ eV.

3.4.3. Complex impedance results.

The complex impedance of a dielectric material can be expressed as follows:

$$Z(\omega) = Z'(\omega) + iZ''(\omega) \tag{9}$$

Fig. 14 illustrates the frequency-dependent behavior of the real part of the impedance, $Z'(\omega)$, at various temperatures. At low frequencies, Z' remains nearly constant, indicating that the material's ac conductivity (σ_{ac}) does not vary significantly in this range. As the frequency increases, Z' begins to decline and eventually stabilizes at a constant value. This reduction at high frequencies is commonly associated with the relaxation of space charge polarization effects.[57]

In Fig. 15, we illustrated the frequency dependence of (Z'') across various temperatures. The Z'' spectra demonstrate an initial increase with frequency across all temperatures, reaching a maximum at the material's characteristic relaxation frequency, ω_{max}, the point where resistance equals reactance. Beyond this frequency, Z'' begins to decline. The observed relaxation peaks are distinct, broad, and asymmetric, indicating a deviation from ideal Debye-type relaxation behavior. With

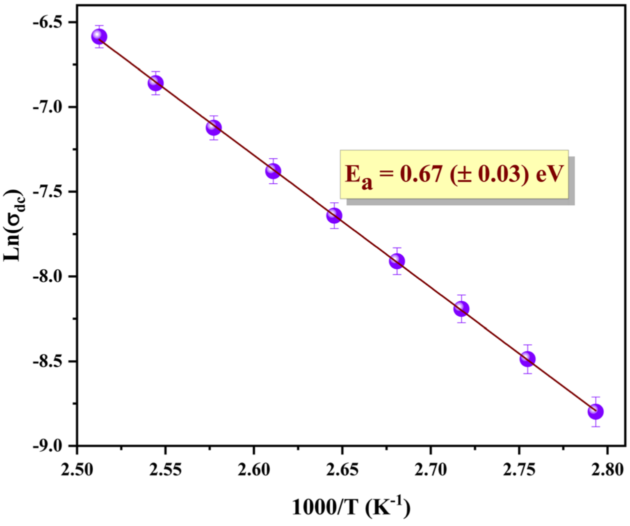

Fig. 13 Evolution of $\ln(\sigma_{dc})$ *vs.* $(1000/T)$.

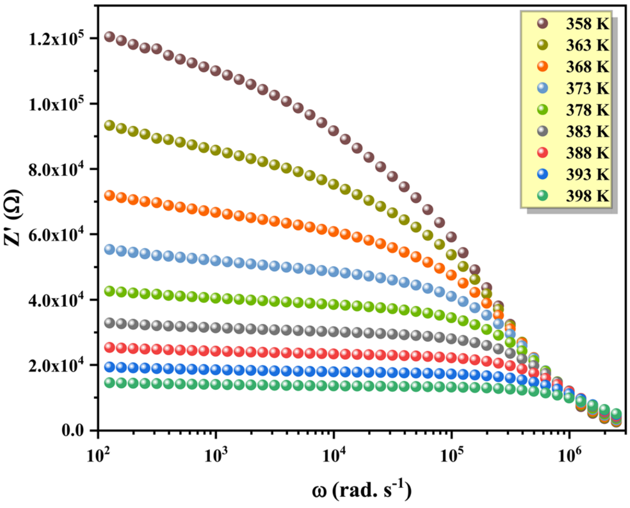

Fig. 14 Frequency evolution of Z' at various temperatures.

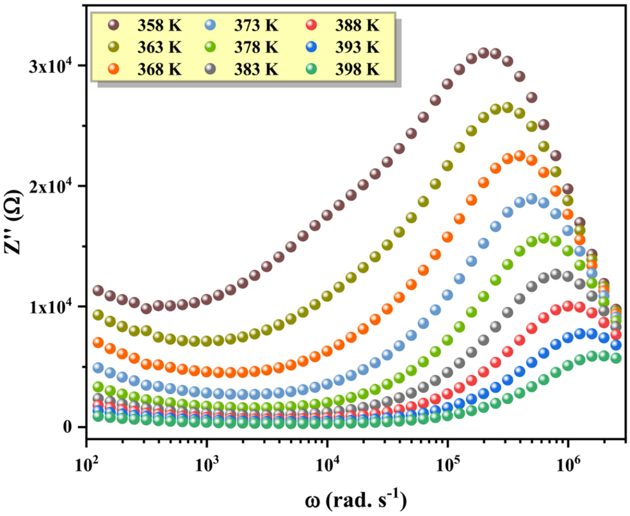

Fig. 15 Frequency evolution of Z'' at various temperatures.

increasing temperature, the height of the relaxation peak diminishes, and the peak shifts toward higher frequencies. This trend confirms that $(C_6H_{10}N_2)(H_2PO_4)_2$ exhibits thermally activated relaxation mechanisms, where the electron-hopping rate accelerates as temperature increases. At elevated temperatures, the relaxation time associated with hopping electrons becomes shorter, making them less able to follow the oscillations of the external field. Consequently, polarization decreases at higher frequencies.[41]

To assess whether the relaxation frequencies of Z' and Z'' coincide, we calculated the derivative $\mathrm{d}(Z'/Z'_{\max})\mathrm{d}\omega$, and plotted its variation with frequency alongside $Z''/Z''_{\max}$ in Fig. 16. The resulting curves clearly show that the relaxation frequencies of Z' and $-Z'$ differ significantly, confirming a departure from the ideal Debye behavior.[58]

The Nyquist plots ($-Z''$ *versus* Z') for the $(C_6H_{10}N_2)(H_2PO_4)_2$ compound, measured at various temperatures, are presented in Fig. 16. These plots reveal the presence of a primary semicircular arc and a low-frequency tail that appears to suggest the onset of a second arc. The first arc corresponds to the grain-boundary response, while the second is attributed to the electrode effects. Notably, the arcs are centered below the real axis, indicating a broad distribution of relaxation times, a hallmark of non-Debye-type relaxation.[59]

Fig. 17 presents the Nyquist plots ($-Z''$ *versus* Z') of $(C_6H_{10}N_2)(H_2PO_4)_2$ recorded at different temperatures. The spectra exhibit a well-defined semicircular arc in the high-frequency region, attributed to the material's intrinsic response. In addition, a second contribution appears in the low-frequency region; however, this arc is not fully resolved and manifests as a partially developed semicircle.

The low-frequency contribution is assigned to the electrode-sample interface rather than to grain effects. In hybrid materials, electrode polarization arises from charge accumulation at the blocking electrodes, producing a large interfacial capacitance and a distinct relaxation process. Because this interfacial relaxation

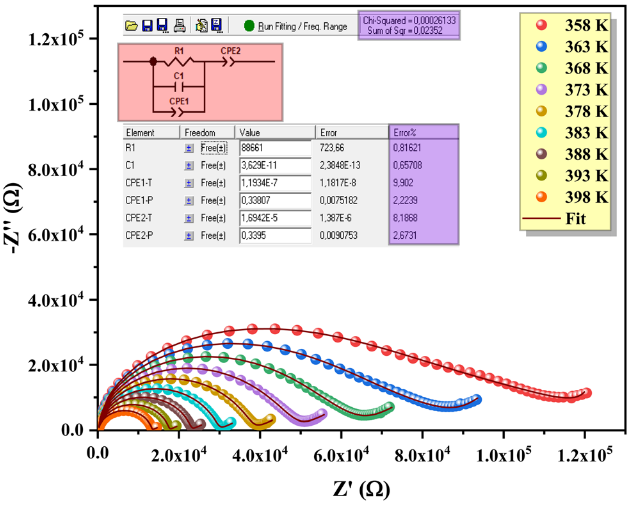

Chi-Squared = 0,00026133
Sum of Sqr = 0,02352

Element	Freedom	Value	Error	Error%
R1	± Free(±)	88661	723,66	0,81621
C1	± Free(±)	3,629E-11	2,3848E-13	0,65708
CPE1-T	± Free(±)	1,1934E-7	1,1817E-8	9,902
CPE1-P	± Free(±)	0,33807	0,0075182	2,2239
CPE2-T	± Free(±)	1,6942E-5	1,387E-6	8,1868
CPE2-P	± Free(±)	0,3395	0,0090753	2,6731

Fig. 17 Nyquist plots of the $(C_6H_{10}N_2)(H_2PO_4)_2$ compound at different temperatures. The inset shows the equivalent circuit and χ^2 value for T = 363 K.

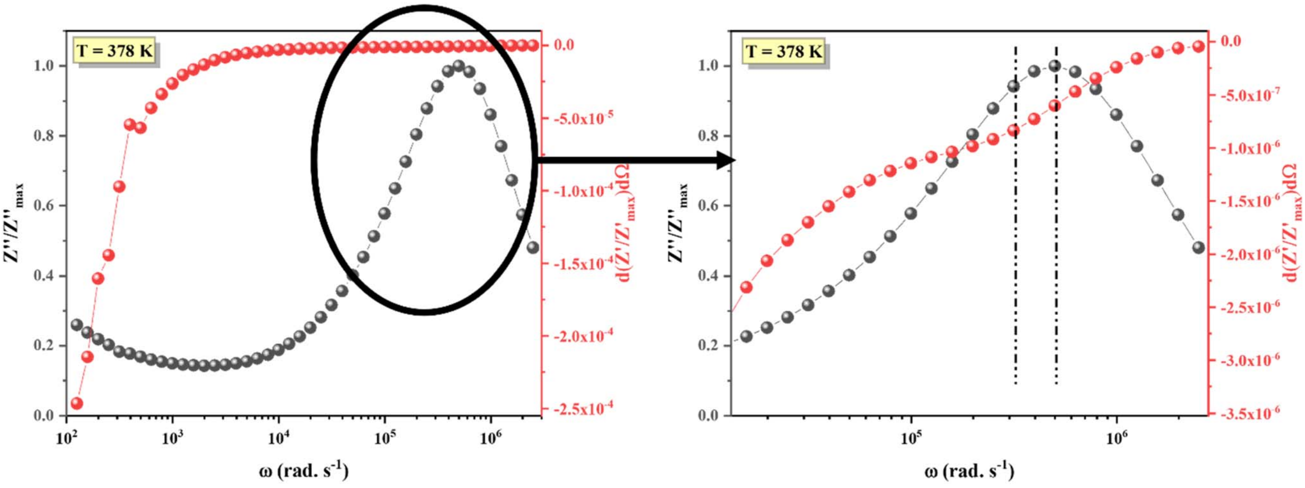

Fig. 16 Frequency evolution of $Z''/Z''_{\max}$ and $\mathrm{d}(Z'/Z'_{\max})\mathrm{d}\omega$.

occurs predominantly at low frequencies and extends beyond the accessible frequency window, only a portion of the corresponding semicircle is observed in the Nyquist representation.

To analyze the impedance data quantitatively, the experimental Nyquist plots were fitted using the ZView software[60] based on a complex nonlinear least-squares (CNLS) method. The fitting procedure was carried out over the entire investigated frequency range to ensure consistency and reliability of the extracted parameters.

The impedance spectra exhibit a depressed semicircular arc at high frequencies, followed by a low-frequency contribution attributed to electrode polarization. To accurately reproduce these features, an equivalent circuit consisting of a grain-boundary resistance (R1) in parallel with a constant-phase element (CPE1) and an ideal capacitor (C1), connected in series with an electrode-related component (CPE2), was employed. The use of a constant-phase element is justified by the non-ideal nature of the semicircular arcs, which indicates a distribution of relaxation times arising from structural heterogeneity and interfacial effects within the hybrid framework.

Several alternative equivalent circuits, including simple R1-CPE1 and R2-CPE2 models, were tested during the fitting process. However, these models either failed to reproduce the depressed character of the semicircle or resulted in physically unrealistic parameter values. The selected R1//C1//CPE1 configuration in series with the electrode contribution provided the best agreement between experimental and simulated data, as confirmed by the low χ^2 (2.6×10^{-4}) (inset of Fig. 17 for $T = 363$ K) values and the excellent overlap between calculated and measured curves in Fig. 17.

The impedance of the CPE is described according to the formulation provided in ref. 61:

$$Z_{\mathrm{CPE}} = \frac{1}{Q(j\omega)^{\alpha}}, (-1 \leq \alpha \geq 1) \tag{10}$$

In this relation, Q represents the capacitance associated with the CPE impedance, while α quantifies the extent of deviation from the ideal Debye behavior. Consequently, the real and imaginary components of the impedance Z can be expressed by the following equations:

$$Z' = \frac{\frac{1}{R_1} + Q_1\omega^{\alpha_1}\cos\left(\frac{\alpha_1\pi}{2}\right)}{\left(\frac{1}{R_1} + Q_1\omega^{\alpha_1}\cos\left(\frac{\alpha_1\pi}{2}\right)\right)^2 + \left(Q_1\omega^{\alpha_1}\sin\left(\frac{\alpha_1\pi}{2}\right) + \omega C_1\right)^2} + \frac{\cos\left(\frac{\alpha_2\pi}{2}\right)}{Q_2\omega^{\alpha_2}} \tag{11}$$

$$Z'' = \frac{Q_1\omega^{\alpha_1}\sin\left(\frac{\alpha_1\pi}{2}\right) + \omega C_1}{\left(\frac{1}{R_1} + Q_1\omega^{\alpha_1}\cos\left(\frac{\alpha_1\pi}{2}\right)\right)^2 + \left(Q_1\omega^{\alpha_1}\sin\left(\frac{\alpha_1\pi}{2}\right) + \omega C_1\right)^2} + \frac{\sin\left(\frac{\alpha_2\pi}{2}\right)}{Q_2\omega^{\alpha_2}} \tag{12}$$

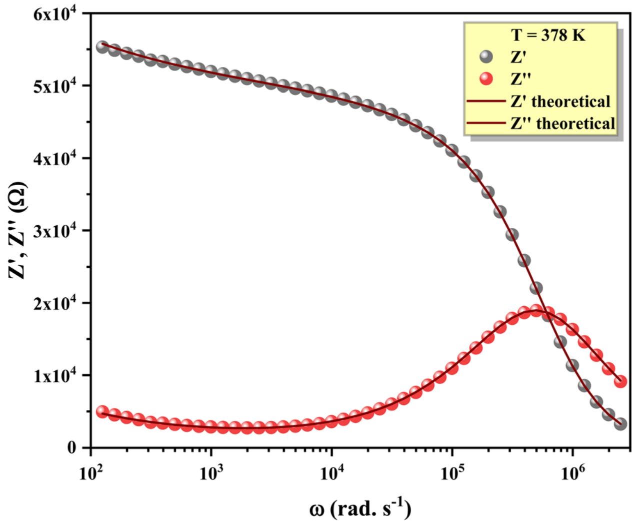

Fig. 18 Frequency evolution of Z' and Z''.

Fig. 18 also demonstrates a strong agreement between the experimental data and the simulated curves of $Z'(\omega)$ and $Z''(\omega)$. The theoretical curves were obtained by fitting the impedance spectra using the Z-View software through a complex nonlinear least-squares procedure based on the proposed equivalent circuit model. The excellent overlap between the experimental and calculated data confirms that the selected equivalent circuit provides an appropriate description of the electrical response of the studied material.

From a structural viewpoint, this non-Debye behavior originates from the heterogeneous nature of the hybrid framework, where inorganic phosphate regions, organic aromatic layers, and hydrogen-bond interfaces contribute differently to polarization and charge transport. This structural complexity results in a broad distribution of relaxation times.

To directly distinguish the different contributions to the conduction process, we calculated the frequency dependence of the phase angle θ of the complex impedance at various temperatures, using the following relation:[58]

$$\theta(\omega) = \tan^{-1}\left(\frac{Z''}{Z'}\right) \tag{13}$$

The corresponding results are presented in Fig. 19. As shown, a single peak appears in the θ spectrum. This peak, located in the low-frequency region, is associated with the grain boundary response.

3.4.4. Complex modulus analysis. The electrical behavior of the $(C_6H_{10}N_2)(H_2PO_4)_2$ compound as a function of frequency at a fixed temperature can also be analyzed through the complex electric modulus M, as defined in ref. 62,

$$M(\omega) = M'(\omega) + iM''(\omega) \tag{14}$$

where M' and M'' represent the real and imaginary parts, respectively.

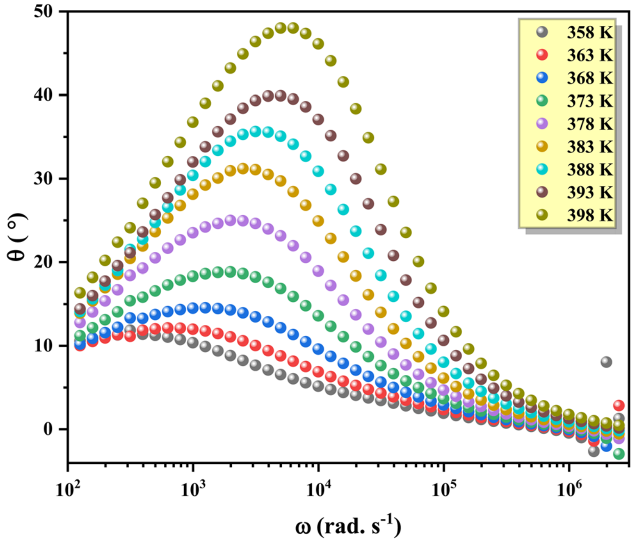

Fig. 19 Bode plots of the phase θ of the complex impedance *versus* frequency at various temperatures.

Fig. 20(a) illustrates the frequency-dependent evolution of M'' at various temperatures for the studied compound. The curves reveal the presence of a single asymmetric relaxation peak at each temperature throughout the entire frequency range. As the temperature increases, the peaks shift towards higher frequencies, indicating a reduction in relaxation time. Using the expression presented in eqn (15), which involves applying the Laplace transformation to the complex electric modulus, the frequency dependence of the M'' data was analyzed:

$$M = M_{\infty}\left[1 - \int_0^{\infty} e^{-i\omega t}\left(\frac{\mathrm{d}\varphi}{\mathrm{d}t}\right)\mathrm{d}t\right] \tag{15}$$

Here, $\varphi(t)$ represents the relaxation function that describes the temporal evolution of the internal electric field E,[63] while M_{∞} ($=1/\varepsilon_{\infty}$) corresponds to the inverse of the high-frequency limit of the real part of the dielectric permittivity.

The asymmetric profiles observed in Fig. 20(a) suggest a non-exponential relaxation behavior, which can be described by a stretched exponential decay function, known as the Kohlrausch–Williams–Watts (KWW) model:[64,65]

$$\varphi(t) = \exp\left[-\left(\frac{t}{\tau_0}\right)^{\beta}\right] \tag{16}$$

In this model, the parameter β ($0 < \beta < 1$) quantifies the deviation from ideal Debye behavior. A value of β approaching 1 indicates Debye-type relaxation, while values closer to 0 imply stronger ionic interactions within the system.

To directly fit the modulus data in the frequency domain, we adopted Bergman's modified version of the KWW model:[66]

$$M''(\omega) = \frac{M''_{\max}}{\left[(1-\beta) + \left(\frac{\beta}{1+\beta}\right)\left[\beta\left(\frac{\omega_{\max}}{\omega}\right) + \left(\frac{\omega_{\max}}{\omega}\right)^{\beta}\right]\right]} \tag{17}$$

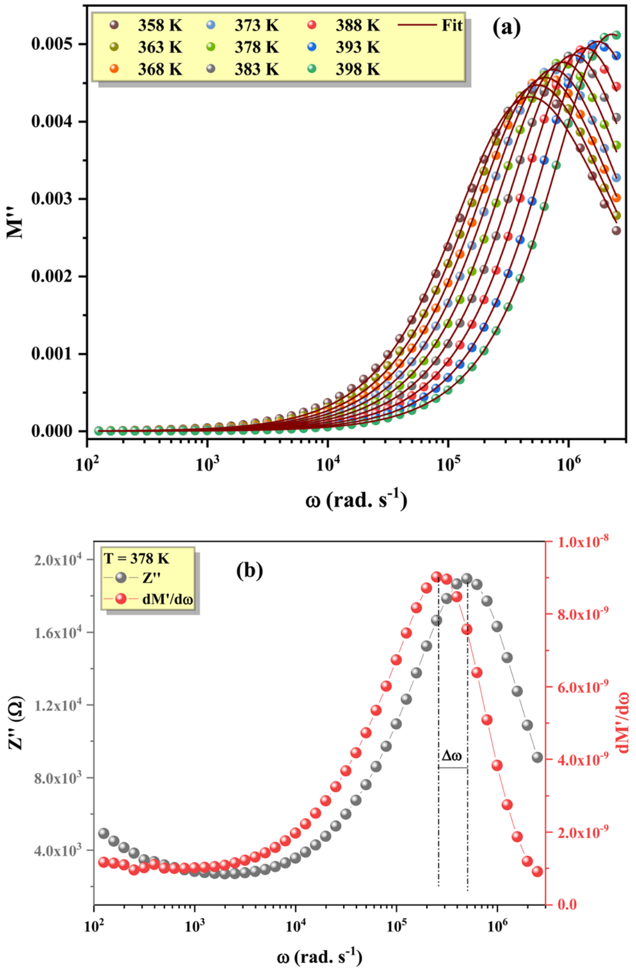

Fig. 20 (a) Complex modulus spectrum as a function of frequency at several temperatures, and (b) frequency evolution of Z'' and M'' at $T = 378$ K.

Here, $M''_{\max}$ denotes the peak value of M'' corresponding to the characteristic frequency $\omega_{\max}$.

The red solid lines in Fig. 20(a) represent the nonlinear fitting of this model to the experimental modulus data. The fitted parameters, summarized in Table 5, show that β values range between 0.67 and 0.87, confirming the dominance of non-Debye relaxation processes in the system.[42]

Additionally, the comparative analysis depicted in Fig. 20(b) demonstrates that the maxima of the Z'' and M'' curves do not coincide for the $(C_6H_{10}N_2)(H_2PO_4)_2$ sample. This observation indicates that the relaxation mechanism is governed by short-range charge carrier motion. The considerable separation between these peaks further supports the non-Debye nature of the relaxation behavior.[42,67–70]

3.4.5. Dielectric study.

The dielectric behavior of a semiconductor material is often characterized using the complex permittivity, as defined by:

$$\varepsilon = \varepsilon' - i\varepsilon'' \tag{18}$$

Table 5 Parameters obtained by fitting the modified KWW function to the frequency-dependent modulus (M″) data

T (K)	$M''_{\max}$ ($\times 10^{-3}$)	β	$\omega_{\max}$ ($\times 10^{6}$ rad s^{-1})
358	4.32	0.67	0.478
363	4.47	0.71	0.553
368	4.57	0.73	0.638
373	4.67	0.76	0.746
378	4.76	0.78	0.898
383	4.86	0.81	1.097
388	4.95	0.83	1.371
393	5.03	0.86	1.753
398	5.13	0.87	2.293

where ε' and ε'' represent the real and imaginary parts, corresponding to the energy storage and energy loss within the material, respectively. These components can be mathematically expressed as follows:

$$\varepsilon' = \frac{Z''}{2\pi f C_0\left(Z'^2 + Z''^2\right)} \tag{19}$$

$$\varepsilon'' = \frac{Z'}{2\pi f C_0\left(Z'^2 + Z''^2\right)} \tag{20}$$

Fig. 21 presents the frequency dependence of the real part of the dielectric permittivity (ε') at different temperatures. Very high ε' values, reaching approximately 10^4 at low frequencies, are observed, which are comparable to those reported for related hybrid systems.[41,42] Such large dielectric constants are commonly associated with Maxwell–Wagner interfacial polarization in heterogeneous systems rather than with intrinsic lattice polarization.[41,71]

In the present compound, the giant low-frequency ε' values are therefore considered predominantly extrinsic in origin. The hybrid crystal structure consists of alternating inorganic dihydrogenophosphate layers and organic aromatic cations linked through an extended hydrogen-bond network. This structural heterogeneity generates internal interfaces between regions of differing conductivity, promoting charge accumulation under an applied electric field. As a result, Maxwell–Wagner polarization develops, leading to an apparent enhancement of the dielectric permittivity at low frequencies.[42,72,73]

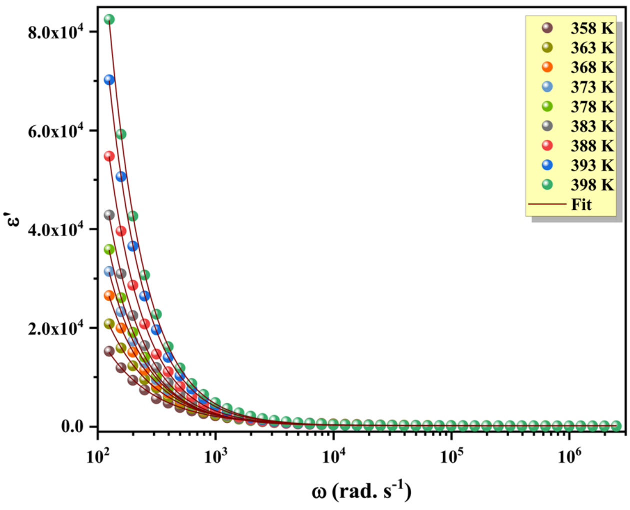

Fig. 21 Frequency evolution of the real part ε' of the dielectric constant at several temperatures.

Additionally, electrode polarization may further contribute in the extremely low-frequency region due to space-charge accumulation at the electrode-sample interface. However, the dominant contribution to the giant ε' values arises from interfacial polarization within the bulk material rather than from intrinsic dipolar or ionic lattice polarization.

As the frequency increases, interfacial charges are no longer able to follow the alternating electric field, and ε' decreases progressively toward a nearly constant value corresponding to the intrinsic dielectric response of the material. This high-frequency plateau reflects the true lattice and dipolar contributions, which are significantly smaller than the low-frequency extrinsic enhancement.[74,75]

The complex dielectric measurements recorded across various temperatures were analyzed using the Cole–Cole model to explore the temperature dependence of dipolar polarization and the associated relaxation mechanisms. The Cole–Cole expression is given by:[76]

$$\varepsilon = \varepsilon_\infty + \frac{\varepsilon_s - \varepsilon_\infty}{1 + (i\omega\tau_0)^{1-\alpha}} \tag{21}$$

The real and imaginary parts of the dielectric permittivity are expressed as:

$$\varepsilon' = \varepsilon_\infty + \frac{(\varepsilon_s - \varepsilon_\infty)\left[1 + (\omega\tau_0)^m \cos\left(\frac{m\pi}{2}\right)\right]}{1 + 2(\omega\tau_0)^m \cos\left(\frac{m\pi}{2}\right) + (\omega\tau_0)^{2m}} \tag{22}$$

$$\varepsilon'' = \varepsilon_\infty + \frac{(\varepsilon_s - \varepsilon_\infty)(\omega\tau_0)^m \sin\left(\frac{m\pi}{2}\right)}{1 + 2(\omega\tau_0)^m \cos\left(\frac{m\pi}{2}\right) + (\omega\tau_0)^{2m}} \tag{23}$$

where ω is the angular frequency, τ_0 denotes the relaxation time, and α is a material-specific parameter representing the degree of relaxation time distribution broadening, with $m = 1 - \alpha$.[77] Here, ε_s and ε_∞ correspond to the static (low-frequency) and high-frequency dielectric constants, respectively.

Eqn (22) was applied to fit the experimental data for the real part of the dielectric constant as a function of frequency (Fig. 21) to determine the dielectric and relaxation parameters of the $(C_6H_{10}N_2)(H_2PO_4)_2$ compound. The extracted parameters from the fitting procedure are presented in Table 6.

The frequency dependence of ε'' for the $(C_6H_{10}N_2)(H_2PO_4)_2$ compound at various temperatures is shown in Fig. 22. The resulting curves exhibit straight lines with nearly identical slopes, which indicates that the σ_{dc} conduction mechanism predominates in this material. As temperature increases, the ε'' values show a marked increase. Furthermore, the frequency variation of ε'' at different temperatures can be analyzed using

Table 6 Extracted fitting parameters obtained from the Cole–Cole equation

T (K)	ε_s ($\times 10^4$)	ε_∞	τ_0 (s)	A
358	1.504	207.20	0.978	0.012
363	2.105	197.13	0.841	0.090
368	2.643	222.29	0.635	0.180
373	3.098	202.30	0.553	0.278
378	3.553	198.92	0.480	0.344
383	4.298	190.94	0.441	0.382
388	5.457	191.53	0.418	0.405
393	7.102	189.12	0.418	0.404
398	8.273	199.12	0.408	0.412

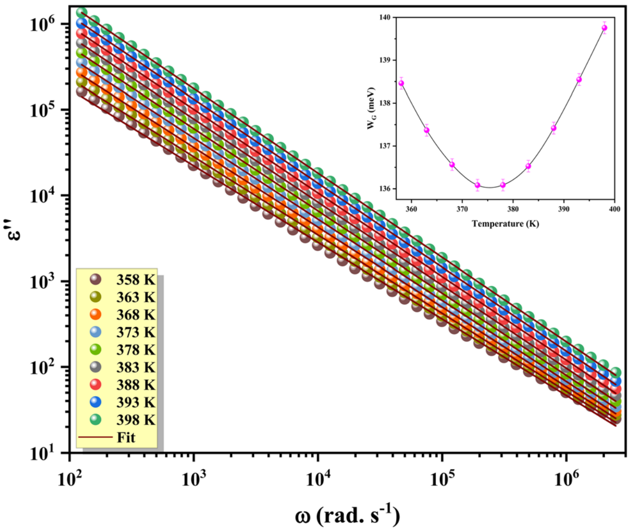

Fig. 22 Evolution of ln(ε″) *versus* ln(ω) at several temperatures. The inset represents W_G values as a function of temperature.

Giuntini's law.[78] The Giuntini equation can be simplified as follows,

$$\varepsilon'' = C(T)\omega^m \tag{24}$$

where $C(T)$ is a temperature-dependent constant and m, defined as $m = 4k_BT/W_G$, is an exponent that characterizes the interaction between electric dipoles. W_G represents the energy required for charge carriers to overcome the potential barrier. To determine the W_G values, we fitted the ln(ε″) *versus* ln(ω) curves to eqn (24), as shown in Fig. 22 for our sample. The extracted W_G values as a function of temperature are presented in the inset of Fig. 21. We found that the variation of m was temperature-dependent. Specifically, in the temperature range of 353–378 K, the exponent m decreased, consistent with the small polaron tunneling model. However, in the intermediate temperature range, m increased, indicating that the correlated barrier hopping (CBH) mechanism becomes dominant. These observations are consistent with our earlier electrical measurements for this material.

Overall, the dielectric behavior of $(C_6H_{10}N_2)(H_2PO_4)_2$ results directly from its crystal architecture. The combination of a hydrogen-bonded phosphate framework, organic–inorganic layering, and internal interfaces creates favorable conditions for interfacial polarization, hopping conduction, and non-Debye relaxation. Therefore, the observed giant dielectric permittivity is not an isolated experimental observation but a direct consequence of the structural organization of the hybrid material, highlighting a clear and meaningful structure–property correlation.

4 Conclusion

This work presents a comprehensive investigation of the synthesis, crystal structure, and functional properties of the hybrid compound *o*-phenylenediammonium bis(dihydrogenophosphate). The material was successfully synthesized and structurally characterized by single-crystal X-ray diffraction, revealing crystallization in the triclinic system with centrosymmetric $P\bar{1}$ space group symmetry. The crystal structure is characterized by alternating organic and inorganic layers, stabilized by an extended network of hydrogen bonds and aromatic interactions.

Optical analysis performed using UV-Visible absorption spectroscopy revealed a direct optical band gap of approximately 2.13 eV, indicating the semiconducting nature of the material and suggesting its potential applicability in optoelectronic devices. Electrical investigations based on complex impedance spectroscopy demonstrated a strong dependence of the electrical response on both frequency and temperature. The thermally activated AC conductivity follows a non-Debye relaxation mechanism consistent with Jonscher's universal power law. Moreover, the asymmetric shape of the imaginary part of the electric modulus, analyzed using the Kohlrausch–Williams–Watts (KWW) formalism, confirms the presence of distributed relaxation processes typical of structurally heterogeneous hybrid materials. The compound also exhibits relatively high dielectric permittivity, highlighting its sensitivity to external electric fields and indicating potential interest for energy storage and conversion applications.

In comparison to previously reported phosphate-based hybrids, the present compound is distinguished by the combination of three key structural features: a strongly connected $(H_2PO_4)^-$ hydrogen-bonded network, π–π interactions between aromatic cations, and an alternating organic–inorganic layered architecture. The cooperative effect of these structural characteristics results in both enhanced dielectric response and semiconducting behavior (band gap = 2.13 eV), demonstrating how control of phosphate connectivity and intermolecular interactions can effectively modulate material properties. These observations highlight that phosphate units play an active role in governing charge transport and polarization phenomena rather than acting solely as passive structural building blocks.

Overall, *o*-phenylenediammonium bis(dihydrogenophosphate) not only contributes to the fundamental understanding of organic–inorganic phosphate hybrids but also demonstrates promising multifunctional properties relevant to electronic, photonic, and energy-related applications. This study provides valuable design insights for future research aimed at exploiting the structural flexibility and tunable physicochemical properties of phosphate-based hybrid materials for advanced technological applications.

Author contributions

Arafet Ghoudi: writing–original draft, validation, software, methodology, investigation. Najoua Weslati: writing–original draft, validation, software, methodology, investigation. Nourah A. Alsobai: writing–original draft, visualization, formal analysis. Noweir Ahmad Alghamdi: writing–review & editing, visualization, validation. Walid Rekik: writing– review & editing, visualization, validation. Abderrazek Oueslati: writing–review & editing, visualization, validation, investigation, formal analysis, data curation.

Conflicts of interest

The authors declare that they have no known competing financial interests or personal relationships that could have appeared to influence the work reported in this paper.

Data availability

The authors confirm that the data used to support the findings of this study are included within the article and are available from the corresponding author upon reasonable request.

CCDC 2359849 contains the supplementary crystallographic data for this paper.[79]

References

1 Z. F. Kanyo and D. W. Christianson, *J. Biol. Chem.*, 1991, **266**, 4264–4268.
2 E. M. Majdi, El Makhloufy, S. Ouasri, A. Saadi, M. El, A. Lahcen and S. Belaaouad, *Mol. Cryst. Liq. Cryst.*, 2021, **714**, 14–25.
3 S. Soukrata, M. Belhouchet and T. Mhiri, *J Clust Sci*, 2015, **26**, 835–849.
4 L. Guelmami, A. Gharbi and A. Jouini, *J. Chem. Crystallogr.*, 2012, **42**, 549–554.
5 H. Dhaouadi, H. Marouani, M. Rzaigui and A. Madani, *Mater. Res. Bull.*, 2008, **43**, 3234–3244.
6 H. Thabet and A. Jouini, *Acta Crystallogr., Sect. C:Cryst. Struct. Commun.*, 1996, **52**, 2248–2250.
7 D. Yu, D. Xue and H. Ratajczak, *J. Mol. Struct.*, 2006, **792–793**, 280–285.
8 D. Xue and S. Zhang, *Chem. Phys. Lett.*, 1999, **301**, 449–452.
9 X. Dongfeng and Z. Siyuan, *J. Phys. Chem. Solids*, 1996, **57**, 1321–1328.
10 R. Kefi and C. B. Nasr, *Anal. Sci.:X-Ray Struct. Anal. Online*, 2007, **23**, x159–x160.
11 E.-E. Bendeif, S. Dahaoui, M. François, N. Benali-Cherif and C. Lecomte, *Acta Crystallogr., Sect. B:Struct. Sci.*, 2005, **61**, 700–709.
12 E. M. Fatila, M. Pink, E. B. Twum, J. A. Karty and A. H. Flood, *Chem. Sci.*, 2018, **9**, 2863–2872.
13 S. Karoui and S. Kamoun, *Mater. Chem. Phys.*, 2026, **350**, 131874.
14 L. Guelmami, M. Dhifet, K. Zaki, N. Alwadai, H. Khmissi, M. Bouzidi, B. Gassoumi and M. Bouachrine, *Front. Chem.*, 2025, **13**, 1701702.
15 S. Bruker and S. SAINT, *Acta Crystallogr., Sect.*, 1990, **46**, 467–473.
16 G. M. Sheldrick, *Acta crystallogr., E*, 2002, 1600–5368.
17 G. M. Sheldrick, *Acta Cryst A*, 2015, **71**, 3–8.
18 L. J. Farrugia, *J Appl Cryst*, 1999, **32**, 837–838.
19 G. M. Sheldrick, *Acta Crystallogr., Sect. C:Struct. Chem.*, 2015, **71**, 3–8.
20 H. Putz and K. Brandenburg, *Cryst. Impact*, Kreuzherrenstr., 102 Bonn, Germany, 53227, 2012.
21 K. Kaabi, C. Ben Nasr and M. Rzaigui, *J. Phys. Chem. Solids*, 2004, **65**, 1759–1764.
22 A. Barhoumi, J. J. Suñol and M. Belhouchet, *J. Mol. Struct.*, 2018, **1173**, 448–455.
23 I. Ben Djemaa, Z. Elaoud, T. Mhiri, R. Abdelhedi and J.-M. Savariault, *Solid State Commun.*, 2007, **142**, 610–615.
24 Z. Elaoud, S. Kamoun, T. Mhiri, F. Romain and H. Burzlaff, *J. Solid State Chem.*, 2000, **155**, 298–304.
25 R. Kefi, C. B. Nasr and F. Lefebvre, *Phosphorus Sulfur Silicon Relat. Elem*, 2007, **182**, 2053–2068.
26 O. Kaman, Ľ. Smrčok, R. Gyepes and D. Havlíček, *Acta Crystallogr., Sect. C:Struct. Chem.*, 2012, **68**, o57–o60.
27 A. Rayes, A. Dadi, N. Mahbouli Rhouma, F. Mezzadri and G. Calestani, *Acta Cryst E*, 2016, **72**, 1812–1815.
28 S. Belghith, Y. Bahrouni and L. B. Hamada, *Open J. Inorg. Chem.*, 2015, **5**, 122–130.
29 C. Janiak, *J. Chem. Soc., Dalton Trans.*, 2000, 3885–3896.
30 N. J. Singh, S. K. Min, D. Y. Kim and K. S. Kim, *J. Chem. Theory Comput.*, 2009, **5**, 515–529.
31 H.-L. Cai and J. Dai, *Acta Crystallogr Sect E Struct Rep Online*, 2010, **67**, o72.
32 R. Altalib, A. Ghoudi, M. Tliha, R. Naouari, W. Rekik, J. Lhoste and A. Oueslati, *RSC Adv.*, 2025, **15**, 33946–33961.
33 H. Elgahami, W. Trigui, A. Oueslati, F. Hlel, M. Belhouchet and M. Gargouri, *J. Iran. Chem. Soc.*, 2021, **18**, 2473–2482.
34 A. Ghoudi, W. Taouali, J. A. Paixão, N. Ahmad Alghamdi, R. Fausto and A. Oueslati, *Mater. Adv.*, 2026, **7**(6), 3231–3246.
35 S. Mtar, N. Chniba-Boudjada, I. Ledoux-Rak, A. Oueslati and M. Boujelbene, *Results Chem.*, 2025, **15**, 102202.
36 J. Tauc, R. Grigorovici and A. Vancu, *Phys. Status Solidi B*, 1966, **15**, 627–637.
37 R. E. Marotti, D. N. Guerra, C. Bello, G. Machado and E. A. Dalchiele, *Sol. Energy Mater. Sol. Cells*, 2004, **82**, 85–103.
38 R. Henríquez, P. Grez, E. Muñoz, H. Gómez, J. A. Badán, R. E. Marotti and E. A. Dalchiele, *Thin Solid Films*, 2010, **518**, 1774–1778.
39 D. K. Hazra, R. Chatterjee, M. Ali and M. Mukherjee, *Acta Crystallogr., Sect. C:Struct. Chem.*, 2010, **66**, o190–o193.
40 R. Hou, C. Shen, H. Chen, L. Meng, L. Xu, J. Wang and D. Wang, *Inorg. Chem.*, 2024, **63**, 803–811.
41 A. Ghoudi, I. Chaabane, R. Naouari, A. Aydi, A. Oueslati, E. Dhahri, B. F. O. Costa, T. Nikitin, J. A. Paixão and R. Fausto, *Inorg. Chem. Commun.*, 2024, **168**, 112925.

42 A. Ghoudi, K. B. Brahim, H. Ghalla, J. Lhoste, S. Auguste, K. Khirouni, A. Aydi and A. Oueslati, *RSC Adv.*, 2023, **13**, 12844–12862.
43 H. Khachroum, M. Krimi, M. S. M. Abdelbaky, S. García-Granda and M. Dammak, *Mater. Res. Bull.*, 2024, **179**, 112978.
44 C. Ben Mohamed, K. Karoui, M. Tabellout and A. Ben Rhaiem, *J. Alloys Compd.*, 2016, **688**, 407–415.
45 D. Abid, I. Mjejri, A. Oueslati, P. Guionneau, S. Pechev, N. Daro and Z. Elaoud, *ACS Omega*, 2024, **9**, 12743–12752.
46 N. Elfaleh, S. Karoui and S. Kamoun, *Indian J. Phys.*, 2022, **96**, 2337–2344.
47 M. Karray, I. Garoui, S. Nasri, N. A. Alsobai, N. A. Alghamdi and A. Oueslati, *Mater. Adv.*, 2025, **7**, 1658–1677.
48 G. E. Pike, *Phys. Rev. B*, 1972, **6**, 1572–1580.
49 A. Ghosh and D. Chakravorty, *J. Phys.: Condens. Matter*, 1990, **2**, 5365.
50 X. L. Cleac'h, *J. Phys. France*, 1979, **40**, 417–428.
51 P. Yadav and A. Sharma, *AIP Conf. Proc.*, 2016, **1728**, 020189.
52 A. Ben Jazia Kharrat, M. Bourouina, N. Moutia, K. Khirouni and W. Boujelben, *J. Alloys Compd.*, 2018, **741**, 723–733.
53 S. R. Elliott, *Adv. Phys.*, 1987, **36**, 135–217.
54 H. Hussein, S. S. Ibrahim and S. A. Khairy, *Mater. Adv.*, 2025, **6**, 2297–2327.
55 S. Karthickprabhu, G. Hirankumar, A. Maheswaran, R. S. Daries Bella and C. Sanjeeviraja, *J. Electrost.*, 2014, **72**, 181–186.
56 K. Funke, *Prog. Solid State Chem.*, 1993, **22**, 111–195.
57 A. Ben Jazia Kharrat, N. Moutia, K. Khirouni and W. Boujelben, *Mater. Res. Bull.*, 2018, **105**, 75–83.
58 R. Mguedla, A. Ben Jazia Kharrat, M. Saadi, K. Khirouni, N. Chniba-Boudjada and W. Boujelben, *J. Alloys Compd.*, 2020, **812**, 152130.
59 M. M. Rahman, N. Hasan, M. A. Hoque, M. B. Hossen and M. Arifuzzaman, *Results Phys.*, 2022, **38**, 105610.
60 F. A. Gulotta, M. A. Montenegro, L. Vergara Diaz, J. Arata Badano, N. F. Ferreyra and V. I. Paz Zanini, *Microchem. J.*, 2023, **190**, 108689.
61 A. Ghoudi, S. Auguste, J. Lhoste, W. Rekik, H. Ghalla, K. Khirouni, A. Aydi and A. Oueslati, *ACS Omega*, 2024, **9**(26), 26339.
62 R. N. Bhowmik and A. G. Lone, *J. Alloys Compd.*, 2016, **680**, 31–42.
63 I. M. Hodge and C. A. Angell, *J. Chem. Phys.*, 1977, **67**, 1647–1658.
64 K. L. Ngai, *J. Non-Cryst. Solids*, 1996, **203**, 232–245.
65 J. Hazarika and A. Kumar, *Synth. Met.*, 2014, **198**, 239–247.
66 R. Bergman, *J. Appl. Phys.*, 2000, **88**, 1356–1365.
67 S. Thakur, R. Rai, I. Bdikin and M. A. Valente, *Mat. Res.*, 2016, **19**, 1–8.
68 I. Gharbi, A. Ghoudi, N. Weslati, M. Tliha and A. Oueslati, *Mater. Adv.*, 2025, **6**, 6358–6369.
69 A. E. Mabrouki, O. Messaoudi, A. Dhahri, A. Azhary, M. Mansouri and L. Alfhaid, *ACS Omega*, 2025, **10**, 22701–22710.
70 R. Meena and R. S. Dhaka, *Phys. B*, 2024, **690**, 416209.
71 I. Gharbi, A. Ghoudi, I. Kammoun, A. Mahmoud and A. Oueslati, *Inorg. Chem. Commun.*, 2024, **166**, 112565.
72 S. Huang, G. Zerihun, Z. Tian, S. Yuan, G. Gong, C. Yin and L. Wang, *Ceram. Int.*, 2014, **40**, 13937–13943.
73 H. E. Sekrafi, A. Ben Jazia Kharrat, M. A. Wederni, N. Chniba-Boudjada, K. Khirouni and W. Boujelben, *J. Mater. Sci.: Mater. Electron.*, 2019, **30**, 876–891.
74 R. S. Devan, D. R. Dhakras, T. G. Vichare, A. S. Joshi, S. R. Jigajeni, Y.-R. Ma and B. K. Chougule, *J. Phys. D: Appl. Phys.*, 2008, **41**, 105010.
75 A. Dutta and T. P. Sinha, *J. Phys. Chem. Solids*, 2006, **67**, 1484–1491.
76 K. S. Cole and R. H. Cole, *J. Chem. Phys.*, 1941, **9**, 341–351.
77 D. Ming, J. M. Reau, J. Ravez, J. Gitae and P. Hagenmuller, *J. Solid State Chem.*, 1995, **116**, 185–192.
78 J. C. Giuntini, J. V. Zanchetta, D. Jullien, R. Eholie and P. Houenou, *J. Non-Cryst. Solids*, 1981, **45**, 57–62.
79 CCDC 2359849: Experimental Crystal Structure Determination, 2026, DOI: 10.5517/ccdc.csd.cc2k6m5l.